Preprint Title	Investigation on drag reduction performance of rotating blade surface with micro-texture
Authors	Qinsong Zhu, Chen Zhang, Fuhang Yu and Yan Xu
Publication Date	19 Jan. 2024
Article Type	Full Research Paper
ORCID® iDs	Qinsong Zhu - https://orcid.org/0000-0001-7674-7205

Investigation on drag reduction performance of rotating blade surface with micro-texture

Qinsong Zhu[1], Chen Zhang*[1], Fuhang Yu[1], and Yan Xu[1]

Address: [1]College of Mechanical and Electrical Engineering, Nanjing University of Aeronautics & Astronautics, Nanjing, 210016, China

Email: Chen Zhang* - meeczhang@nuaa.edu.cn

* Corresponding author

Abstract

For enhance the aerodynamic performance of aero engine blades, the parameters and drag-reduction mechanism of micro-texture to reduce blade surface flow loss are investigated in this study. First, a simplification simulation method is proposed to reduce the calculation cost and determine the aerodynamic parameters of the blade model through the comparison of flow field characteristics and parameters of the blade simulation result. Secondly, the placement position and geometrical parameters of micro-texture with lower energy loss are determined by CFD (Computational Fluid Dynamics) simulation for the established micro-texture on the blade surface and the drag reduction mechanism is analyzed based on the simulation result. The triangular rib with a depth of 0.2mm and width of 0.3mm has the best drag reduction performance, and this micro-texture has an energy loss coefficient reduction of 1.45% and a drag reduction of 1.31% on a single blade. Finally, the blades with the optimal micro-texture

parameters are tested in the intermittent wind tunnel. The experimental results show that the micro-texture decreases the energy loss by 3.7% of a single blade under the working conditions of 57° attack angle and 136.24m/s, which is pleasing for the drag reduction performance of the integral impeller with 45 blades.

Keywords

micro-texture; CFD simulation; simplification method; drag reduction; blade

Introduction

Modern aero-engines have the characteristics of high rotation speed and large flow. The turbulent flow near the wall results in a substantial increase in frictional resistance, dramatically increasing the energy consumption of the entire engine system. Therefore, it holds immense significance for advancing engines to focus on reducing blade surface friction, mitigating turbulence pulsation, and enhancing the aerodynamic performance of the blades [1].

The micro-textured surface of object is inspired by the minuscule groove-like scales found on the sharkskin [2,3]. This biomimetic design feature is particularly effective in reducing resistance during swimming, contradicting the longstanding conventional wisdom that smoother surfaces offer less resistance obsolete. Therefore, numerous scholars began to research the drag reduction performance of micro-textures based on the idea of bionics [4].

In 1982, Walsh et al. [5]. from NASA Langley Laboratory conducted a pioneering micro-texture study on surfaces. Their experiments focused on longitudinal grooves with various shapes, revealing that symmetrical V-shaped grooves exhibited a remarkable drag reduction effect at low flow rates. The highest degree of optimal drag reduction

attained was 8%. Bechert et al. [6] pointed out that the reduction of transverse velocity fluctuation near the rib, which contributed to drag reduction. They introduced the concept of "Protruding Height", indicating that micro-texture increases the thickness of the boundary layer, thereby decreasing the average velocity gradient of the wall and mitigating resistance between the fluid and wall. Huang [7] studied the micro-structure resistance from the perspective of the turbulent boundary layer and affixed tiny bumps on the aircraft wing surface to achieve a resistance rate of 7%. Martin [8] explored the continuous and segmented longitudinal ribs, revealing that the ribs effectively impede the transverse expansion of the vortex and reduce shear stress, thereby reducing resistance. Furthermore, segmented ribs exhibited better drag-reduction characteristics as they lifted the vortex structure. Bearman et al. [9] designed a cylinder surface covering semi-circular pits, and experimental results demonstrated the effective flow resistance reduction within a certain *Re* (Reynolds number) range. Choi [10] positioned miniature sensors at the bottom of micro-textures and verified the effect of riblets on reducing wall pulsation pressure through wind tunnel experiments. Bixlei et al. [11] arranged non-smooth structures in a closed channel and conducted experiments by varying the geometry of the structures, fluid flow velocity, and fluid viscosity. The results demonstrated that non-smooth structures reduce pressure drop in the flow process and achieve drag reduction effect. Mayoral and Jimenez [12,13] used the direct numerical simulation (DNS) method to explain that the viscous region on two-dimensional ribs experiences cracking, and the drag reduction effect caused by the ribs changes linearly with the transverse spacing of the ribs. In addition, they compared drag reduction rates of fluid at *Re*=550 and *Re*=180, observing minimal differences and concluding that the drag reduction rate is less dependent on the Re.

In recent years, a growing number of scholars have been studying the application of micro-texture on curved surfaces. Early studies mainly focused on experiments, but

due to limitations related to experimental equipment and costs, these studies often involved simple rotating bodies or pipelines. In contrast, recent research has witnessed many researchers placing micro-textures on the turbine blade surfaces, including aircraft wings, fans, compressors, and more. They have explored the drag reduction effect and mechanism through the utilization of numerical simulation technology. Chamorro [14] studied fans with a grooved surface and found that in certain operating conditions, the drag reduction effect of local coverage on the textured blade surface surpassed that of overall covering. Additionally, they designed micro-grooves of various sizes on the suction surface to achieve the optimal drag reduction effect. Zhang et al. [15] proposed a method to determine the placement position of micro-textures by using finite element analysis. The micro-texture was arranged on the blade surface, which exhibited a better drag reduction effect than the smooth blade.

As can be seen from the abovementioned summary of micro-texture surface drag reduction techniques, scholars have achieved many achievements. They conducted numerous studies encompassing the design, application, experimental verification, and drag reduction mechanism exploration of micro-texture. However, there are still a few problems to be explored:

(1) The numerical simulation is inconsistent with the actual working condition.

Most research objects are flat plates or simple spinning bodies at low velocities. There are few studies about the drag reduction performance of complex micro-texture surfaces under high-speed flows. Some scholars have employed static single-channel simulations for a single airfoil without considering the rotation of blades. It is necessary to establish the relationship between individual blades and rotating impellers.

(2) The drag reduction mechanism of micro-texture on the blade surface is difficult to analyze in wind tunnel experiments.

Conventional wind tunnel experiments are constrained by the small size of micro-textures, making it challenging to observe their effects on the microscopic surface flow. As a result, various theories related to drag reduction on planar surfaces have been proposed by scholars based on finite element simulation. However, theories on complex surfaces still need to be clarified, especially on impeller blades.

Theoretical background

Boundary layer theory

As shown in Figure 1, the fluid near the wall at the front end of the flat plate is laminar. However, the flow in the boundary layer will gradually transform to turbulent as the fluid flowing along the flat plate. It is need to note that this transformation occurs gradually, and there is no distinct boundary line between the laminar and turbulent flow regions.

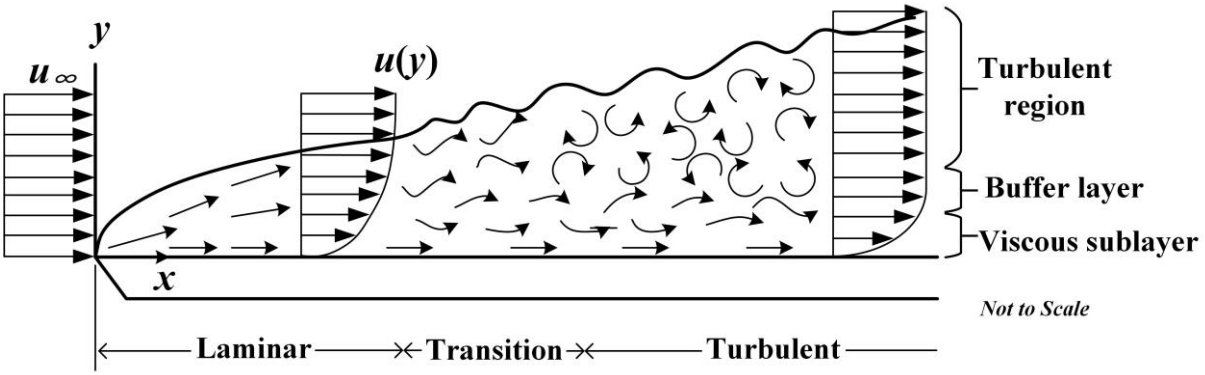

Figure 1: Development of the boundary layer on near wall surface.

The near-wall region within the boundary layer is the primary source of turbulent kinetic energy. This region can be divided into three distinct regions: the viscous sublayer, the buffer layer, and the log law region. The position of each region within the boundary layer is determined based on the dimensionless distance from the wall [16-18]:

$$y^+ = \frac{yu_\tau}{v} \quad (1)$$

where y^+ is the dimensionless distance from the wall, y is the distance from the wall, u_τ is the wall stress shear velocity, v is the kinematic viscosity of the fluid [19]. According to Figure 2, the near-wall area is usually in the range of $y^+ \leq 100$. The range of the viscous sublayer region is $0 \leq y^+ \leq 5$, where the viscous shear stress is dominant and the turbulent shear stress is zero. The buffer layer is $5 \leq y^+ \leq 30$, characterized by the simultaneous presence of both viscous and turbulent shear stresses. The overlap layer ranges from $30 \leq y^+ \leq 100$, where the turbulent shear stress becomes dominant. [20].

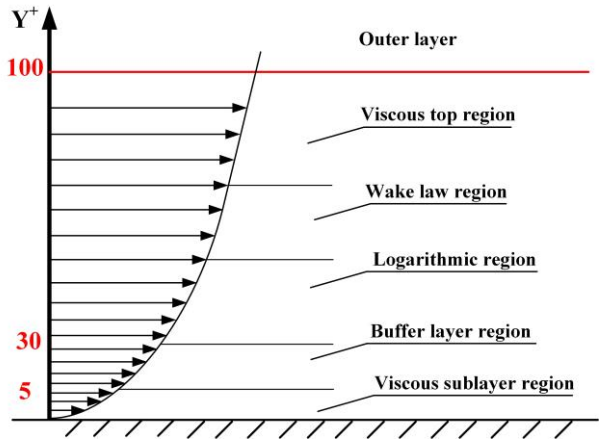

Figure 2: The schematic diagram of boundary layer stratification.

The turbulence within the boundary layer forms a fluid structure called the coherent structure, which can be divided into different types, including vortex, blast, and sweep [21]. Robinson [22] proposed an idealized schematic diagram of vortex structures in different regions of the turbulent boundary layer. The flow vortex is prominent in the buffer sublayer, while the hairpin vortex prevails in the outer layer. These two types of vortices overlap within the logarithmic region.

The velocity gradient in the vicinity of the wall intensifies due to the vortices, thereby generating a transverse shear force that contributes to heightened resistance. Thus, the control of vortices becomes advantageous in achieving a surface with reduced resistance. By analyzing the behavior of vortices, the design of micro-textures aims to facilitate vortex uplift, reducing shear stress and attaining a surface exhibiting lower resistance.

Drag reduction performance formula

The total resistance (F) of the blade is mainly composed of two parts: pressure drag (F_p) caused by the pressure gradient and frictional drag (F_f) caused by the viscous of the wall. Their relationship is shown as follows:

$$F = F_p + F_f \tag{2}$$

Therefore, the drag reduction rate (DR) for the blade surface can be expressed as follows:

$$DR = \frac{F_0 - F_1}{F_0} \times 100\% \tag{3}$$

where F_0 and F_1 are the total resistance on the smooth blade and micro-textured blade, respectively. Then the change rate of energy loss coefficient (η_ξ) and total pressure loss coefficient (LC_{TP}) are used to represent the change of resistance of the blade and flow path to improve the reliability of the results [23], as shown in the following formula:

$$\eta_\xi = \frac{\xi_1 - \xi_0}{\xi_0} \times 100\% \tag{4}$$

where ξ_0 and ξ_1 are the energy loss coefficient of the smooth blade and micro-textured blade, respectively. The energy loss coefficient ξ is defined as:

$$\zeta = \frac{h_{1s}^* - h_1}{h_{1s}^*} = \frac{\left(P_2/TP_2\right)^{\frac{k-1}{k}} - \left(P_2/TP_1\right)^{\frac{k-1}{k}}}{1 - \left(P_2/TP_1\right)^{\frac{k-1}{k}}} \tag{5}$$

where TP_1 and TP_2 are the total pressure on the inlet and outlet of the cascade flow, respectively; P_1 and P_2 are the static pressure on the inlet and outlet of the cascade flow, respectively; k is the specific heat ratio and the air is 1.4. And the LC_{TP} can be expressed as:

$$LC_{TP} = \frac{TP_2 - TP_1}{TP_1} \tag{6}$$

The total pressure (TP) is equal to the sum of dynamic pressure (DP) and static pressure (P), which can be calculated by the following equation:

$$TP = P\left(1 + Ma^2 * (\frac{k-1}{2})\right)^{\frac{k}{k-1}} \tag{7}$$

where Ma is Mach number, Ma is defined as:

$$Ma = V/C \tag{8}$$

where V is the airflow velocity, speed of sound C is defined as:

$$C = \sqrt{kTR} \tag{9}$$

where T is absolute temperature, R is gas constant. In this paper, the value of T and R are 300 K and 287, respectively.

The η_ξ represents the change of energy consumption of the whole system. The higher η_ξ indicates the increase of energy consumption of the system, indicating that micro-texture has an adverse effect on the aerodynamic performance of the blade.

Modeling of micro-textures on blade surface

The compressor with 45 blades is studied in this paper, the impeller radius and blade height are 300mm and 110mm, respectively. The micro-texture on blade surface can bring drag reduction performance but this performance depends on the position and size of the micro-texture. In general, micro-textures do not need to cover the blade surface completely. It is necessary to determine the position of the micro-texture

according to the flow condition on smooth blade surface, and determine the size of the micro-texture through theoretical calculation.

Obtaining the flow condition on smooth blade surface

To obtain the flow condition of smooth blade surface accurately and determine the position of the micro-texture, a new method of simplified numerical simulation for micro-textures on rotating blade surfaces is proposed in this paper. The flow diagram is shown in Figure 3.

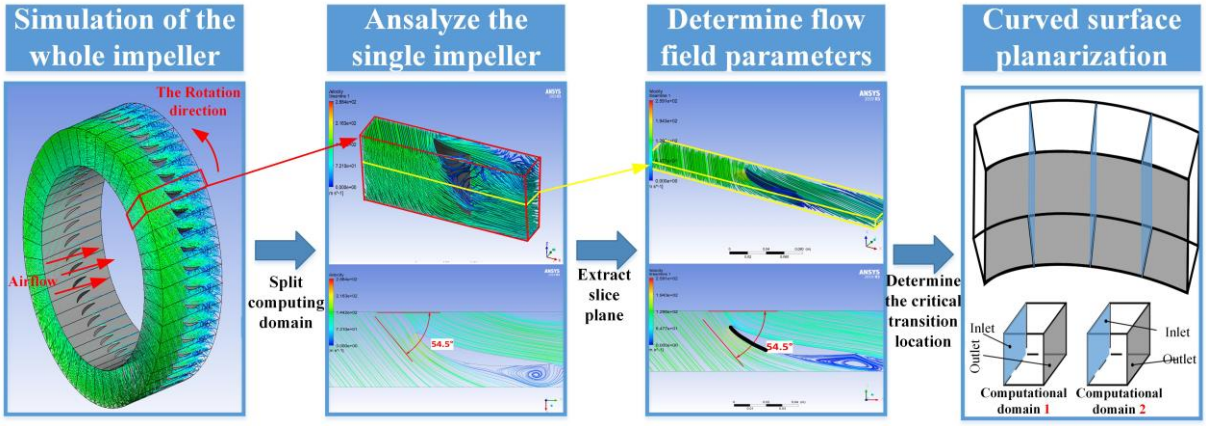

Figure 3: Flow chart of simplified numerical simulation method. Images used courtesy of ANSYS, Inc.

Step 1: The numerical simulation of the whole impeller without micro-texture is carried out in *Ansys® CFX, Release 2020 R2*. In simulation setup, the Realized *k*-epsilon (*k*-*ε*) model with enhanced wall treatment is adopted for the turbulence modeling [24]. The Realized *k*-*ε* model has better prediction results for rotation, boundary layer separation with large back pressure gradient and backflow phenomena. The boundary conditions are set according to the working conditions of impeller. The inlet is defined as a velocity inlet with a magnitude of 75 m/s, while the outlet is a pressure outlet with a value of 101325 Pa. The periodic boundary conditions are applied on both sides of

the flow domain, and the upper and lower walls are no-slip walls. The rotational speed of impeller is 2880r/min.

As a rotating machine, the flow through each impeller blade is periodic. Thus, the 45-stage impeller is divided evenly, and each blade occupies an 8° fan-shaped flow channel space, as shown in Figure 4. The flow channel has a length of 300mm, while the bottom and top radii of the blades measure 300mm and 410mm, respectively. According to the above impeller parameters, we use the speed triangle [25] to calculate the theoretical value of the 0.5 blade height. The relative airflow velocity is determined to be 130.67m/s, with an attack angle of 54.97°.

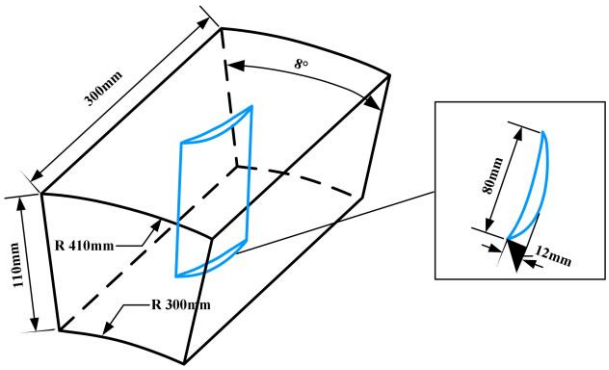

Figure 4: Calculate domain size and the single blade size parameters.

Step 2: The simulation results analysis of the single impeller. We analyze the result to determine the flow field characteristics around the single blade, such as the angle of attack, velocity, air flow state, and other parameters. As shown in Figure 5 (a), we slice the calculation domain to analyze the simulation results better and select the plane at the 0.25 position (green surface) from the inlet to the outlet. In the radial direction, three curved surfaces with spans of 0.25, 0.50, and 0.75, progressing from the bottom to the top, are chosen for analyzing the velocity distribution at the intersection between these curved surfaces and the green plane. The result from Figure 5 (b) indicates an increase in the peripheral speed of the blade as the radius increases. The average velocity at

Span=0.5 blade height is 131.5m/s, with an error of only 0.6% from the theoretical value of 130.67m/s. This result serves as evidence supporting the reliability of the simplified simulation method, so the velocity in the local area simulation is set at 130.67m/s.

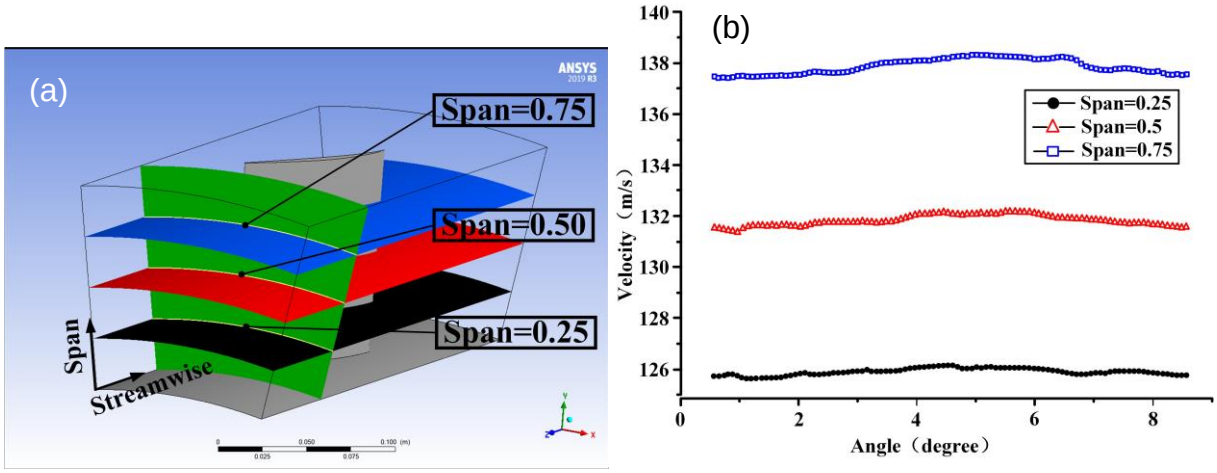

Figure 5: The single blade and simulation result. (a) Slice location of the calculation domain. (b) The simulation result of flow velocity at Span=0.25, Span=0.5, and Span=0.75. Figure 5 (a) used courtesy of ANSYS, Inc.

In Figure 6, two-dimensional flow streamlines of the expansion surface are analyzed at span=0.25, 0.5, and 0.75. The relative velocity of the airflow concerning the blades varies as the blades rotate. Furthermore, an increase in both the velocity and the relative velocity angle between the airflow and the blades is observed as the distance from the *h*) hub to the shroud increases. The comparison of simulation results is shown in Table 1. The flow velocity and attack angle at span=0.50 are selected as the initial conditions for subsequent simulations.

Table 1: Attack angle comparison of simulated and theoretical values.

Surface	Simulation values (°)	Theoretical values (°)	Error (°)
Span=0.25	52.3	52.8	0.95

Span=0.50	54.8	54.97	0.31
Span=0.75	56.5	57.0	0.88

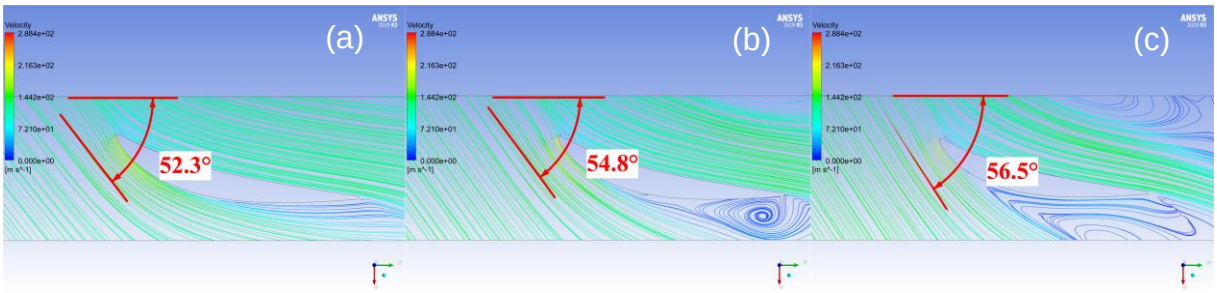

Figure 6: Simulation values of attack angle at (a) Span=0.25, (b) Span=0.50, and (c) Span=0.75. Images used courtesy of ANSYS, Inc.

Step 3: Construction of the relation between curved surface and plane. The blade is a curved surface with a complicated flow situation, but in areas without boundary layer separation on the blade surface, the flow conditions resemble those on a plane. Figure 7 shows the schematic of flow around the airfoil surface, where point A is the stagnation point, point B is the highest point, and point C is the separation point. The region between A and B is the barotropic region, characterized by smooth airflow along the wall without boundary layer separation. Therefore, this region is discretized and treated as a collection of small local planes. Conversely, the pressure difference after point C triggers flow reversal and separation of the boundary layer from the wall, resulting in a vortex zone known as the separation region. The generation of the separation region significantly impacts the outflow boundary, thereby relieving the influence of viscosity on the thin fluid layer near the wall.

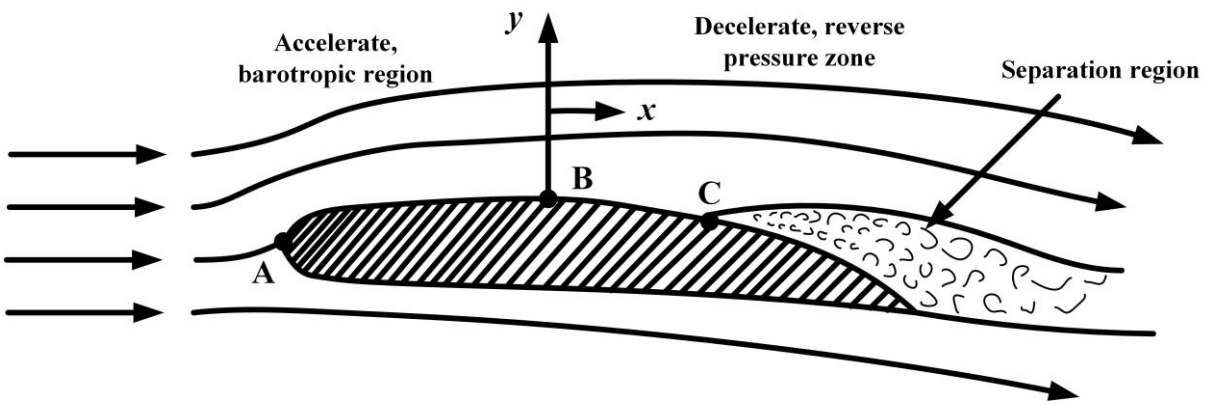

Figure 7: The schematic diagram of boundary layer separation on airfoil surface**.**

Thus, we planized the barotropic region to establish the relationship between the plane and the curved surface to explore the application of micro-textures for drag reduction on curved surfaces. Moreover, the flow parameters of single-ring blades determined from Step 1 and Step 2 are applied to the plane, minimizing the simulation result errors.

Determination of micro-structure position

Thus, according to the above steps, the air attack angle and flow velocity at span=0.50 are 54.97° and 130.67m/s, respectively. This condition is used to study the flow on the blade surface and determine the micro-texture position.

In order to simulate the actual flow field accurately, the inlet and outlet boundary conditions are set as velocity inlet and pressure outlet, respectively. The flow velocity is 130.67m/s, the attack angle is 54.97°, and the outlet pressure is 101325pa. Considering the amount of calculation, the upper and bottom walls are set as symmetrical boundaries, with a Z-axis thickness kept as small as possible. At the same time, providing enough space to develop a vortex along the span direction is essential. Hence, a thickness of 10mm is chosen, allowing for the inclusion of 10 grooves, each 1mm wide. The boundary conditions on the left and right sides are periodic, as shown in Figure 8.

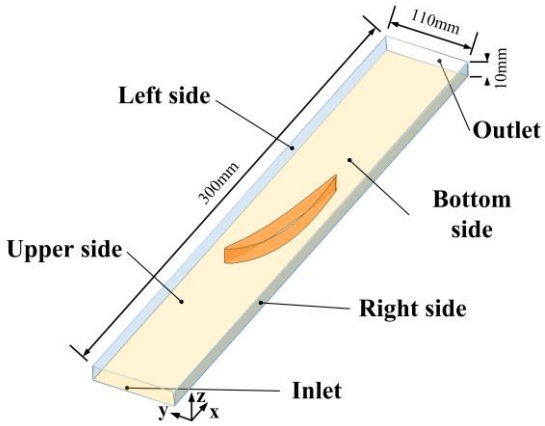

Figure 8: Flow domain model of the blade.

Due to the irregular curved shape of the blade surface and the relatively small scale of the micro-textures, an unstructured mesh is used to generate the computational domain mesh. The turbulence models have strict requirements on the first layer mesh size, known as y^+. In order to ensure compatibility between the mesh quality and the turbulence model, the y^+ value needs to fall within the range of 1 to 5 [26]. In this paper, the height of the first layer mesh is 0.005mm, and y^+=1.5 correspondingly.

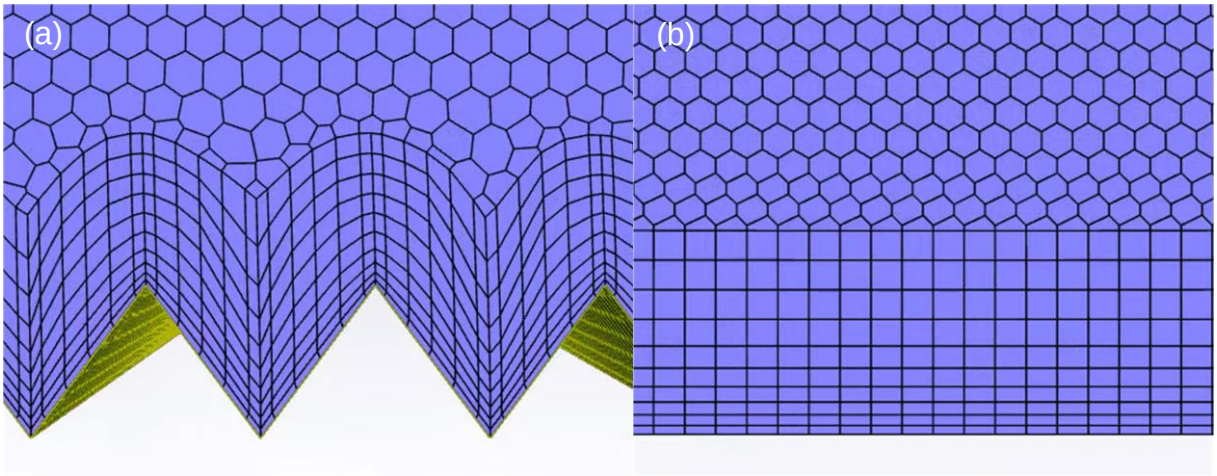

Figure 9: Local mesh refinement of (a) microstructure surface and (b) smooth surface. Images used courtesy of ANSYS, Inc.

This paper selects the Realized *k-ε* turbulence model in the *Ansys® Fluent, Release 2020 R2*. The wall function is introduced to address the region near the wall with a low *Re*（Reynolds number）. The enhanced function is chosen because it considers the influence of specific wall fluid viscosity and applies to the flow near the wall with low *Re*. The second-order upwind scheme is adopted to discretize the equation, and the SIMPLE algorithm is used for iterative calculation [27].

As shown in Figure 10, the flow fields of the pressure and suction surfaces exhibit significant variations. Regarding pressure distribution, the pressure surface is notably more significant than the suction surface, especially at the leading edge of the blade. The pressure increases along the positive X direction of the suction surface, accompanied by an apparent shock wave in front of it. However, the pressure stabilizes towards the back end of the blade.

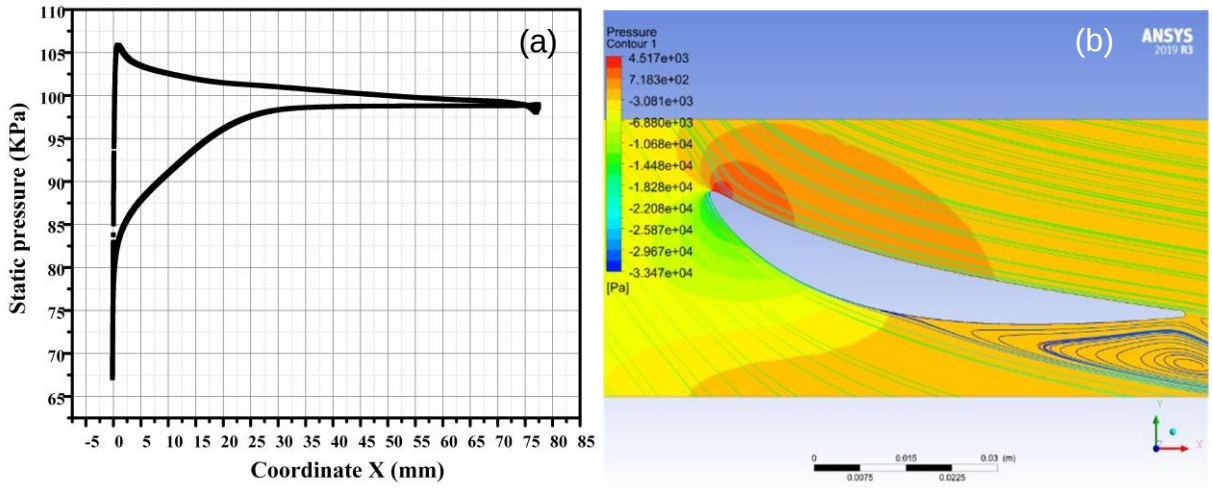

Figure 10: The distribution of (a) the static pressure and (b) the flow field on the blade surface. Figure 10 (b) used courtesy of ANSYS, Inc.

Table 2 presents the resistance results of the smooth blade, where the total drag (T_d) in the direction of airflow is divided into pressure drag (P_d) and friction drag (F_d). The primary impact of micro-texture is to modify the flow state of the boundary layer near

the wall, reducing of F_d. For our blade, the contribution of F_d is small, accounting for only 2.39% of the T_d. Thus, this paper primarily focuses on assessing the influence of micro-texture on system energy loss.

Table 2: Aerodynamic parameters of the smooth blade.

Type	P_d (N)	F_d (N)	T_d (N)	F_d / T_d (%)
Smooth	1.3288	0.0325	1.3613	2.39

The pressure surface exhibits a favorable pressure gradient from the leading edge to the trailing edge of the blade, whereas the suction surface presents an adverse pressure gradient. This observation is complemented by Figure 11, which illustrates that the Turbulent Kinetic Energy (k) on the blade surface is minimal. Observing the distribution of k on the periodic boundary shows that k is zero in the front region of the blade (X≤ 0mm). However, k begins to rise sharply at the start from X=40mm, indicating that boundary layer separation at this position generates turbulence. The peak of k indicates that this position corresponds to the center of the turbulent vortex. According to Figure 10 (b), the turbulent vortices manifest on the suction surface within the system. Therefore, the micro-texture is arranged on the suction surface in this paper.

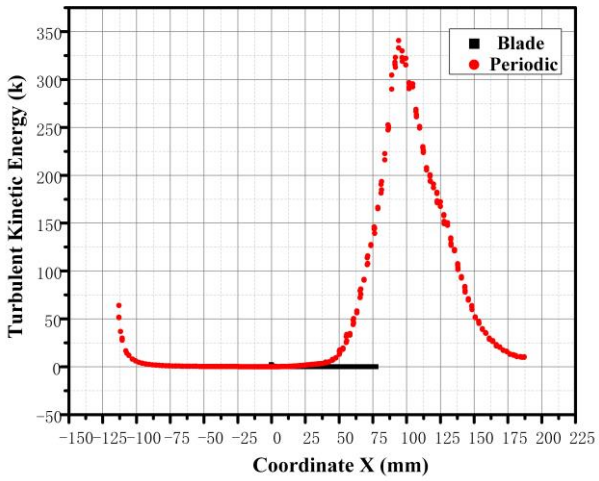

Figure 11: Distribution of turbulent kinetic energy on blade surface.

Based on Figure 11, the boundary layer initiates separation at X=30mm. As a result, the suction surface can be divided into two regions (front and back) at X=30mm, which serves as the critical point to discuss the drag reduction performance of the micro-texture.

Dimensionless parameters of micro-structures

The method of dimensionless size is used to determine the size range of micro-textures with drag-reducing properties [28]. In this section, the micro-texture sizes are determined according to the boundary theory, mainly including the height (*h*), width (*w*), and spacing (*s*), as shown in Figure 12.

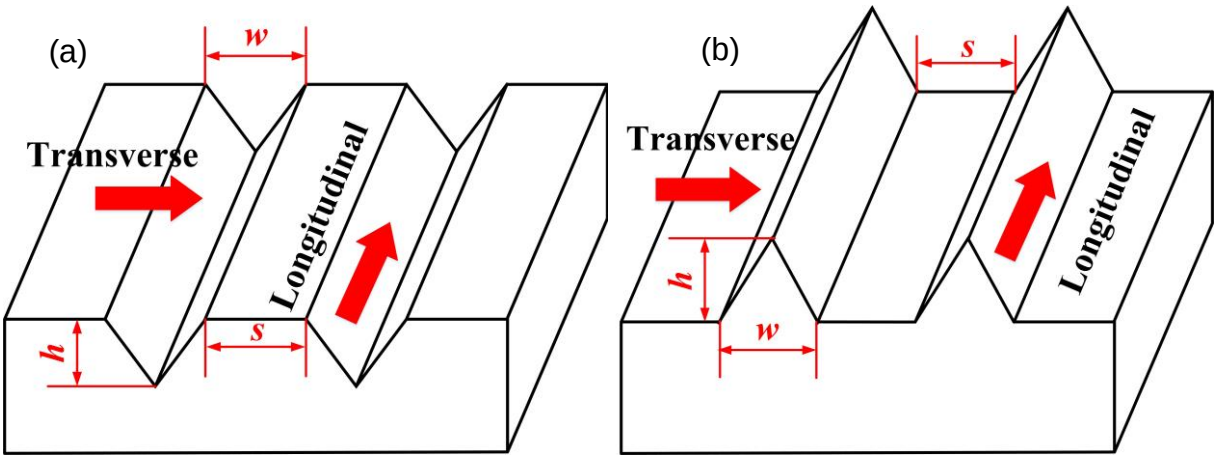

Figure 12: Characteristic parameters of (a) grooves and (b) ribs.

The dimensionless parameter calculation formula of micro-texture is shown as follows [29]:

$$s^+ = \frac{su_\tau}{v} \tag{10}$$

$$h^+ = \frac{hu_\tau}{v} \tag{11}$$

$$w^{+}=\frac{wu_{\tau}}{v} \tag{12}$$

$$u_{\tau}=\left(\frac{\tau_{w}}{\rho}\right)^{1/2} \tag{13}$$

where μ is the dynamic viscosity, v is the kinematic viscosity, u is the average flow velocity, u_τ is the wall stress shear rate, τ_w is the wall shear stress, ρ is the density.

$$\mu=\rho v \tag{14}$$

$$\tau_{w}=0.0225\rho u^{2}\left(\frac{v}{u\delta}\right)^{1/4} \tag{15}$$

The flow condition around the flat plate wall can be determined by the dimensionless number (the local Reynolds number) $Re_x=\frac{\rho u_0 x}{\mu}$, where x is the distance from the inlet along the fluid flow direction, and u_0 is the flow velocity. In the range of $Re_x<3\times10^5$, the flow in the boundary layer is laminar and the following equation can calculate the thickness of the boundary layer δ:

$$\delta=4.96\times\left(\frac{v}{ux}\right)=4.96\times Re_{x}^{-1/5} \tag{16}$$

The flow is turbulent if the range of $Re_x>3\times10^6$, and the thickness of δ is calculated as:

$$\delta=0.37\times\left(\frac{v}{ux}\right)=0.37\times Re_{x}^{-1/5} \tag{17}$$

The flow in the boundary layer is transitional when Re_x is between 3×10^5 and 3×10^6. The complete turbulent area is selected to arrange micro-texture. Therefore, substituting the Eq. (17) into (15):

$$\tau_{w}=0.029\rho u^{2}\left(Re_{x}\right)^{-1/5} \tag{18}$$

Substituting the Eq. (18) into (13):

$$u_\tau = 0.17uRe_x^{-1/10} \tag{19}$$

Substituting the Eq. (19) into (10), (11), and (12), respectively:

$$s^+ = \frac{0.17suRe_x^{-1/10}}{v} \tag{20}$$

$$h^+ = \frac{0.17huRe_x^{-1/10}}{v} \tag{21}$$

$$w^+ = \frac{0.17wuRe_x^{-1/10}}{v} \tag{22}$$

Based on the above equations, we can establish limitations on the size range of micro-textures, offering valuable guidance for designing such structures. Furthermore, it is imperative to consider other factors including type, direction, location, quantity, etc. The specific parameters are shown in Table 3.

Table 3: Micro-texture parameters.

Parameters	Value
Direction	Spanwise, Longitudinal
Type	Groove, Rib
Height (h)	$5 < h^+ < 30$[5]
Width (w)	$< 3h$
Spacing (s)	$< 3h$
Position	Front, Back

Results and Discussion

This chapter is written in two parts. The first one presents the simulation results of different micro-textures arranged on blade surface. Through the discussion of 10 sets of simulation results, the optimal combination of micro-texture parameters with the best drag reduction performance is determined, which is then applied to the actual blade surface for experiments. The second one discusses the drag reduction mechanism of the micro-texture based on the simulation results.

Construction and discussion of micro-structures

Construction and comparison of different micro-structures

To explore the effect of micro-texture on the flow field and resistance, the groove and rib are arranged at the front and back sections of the suction surface, respectively, as shown in Figure 13. According to the flow field information on the smooth blade, the velocity in the front section of the suction surface is faster. The placement of ribs here increases the projection area, resulting in the increase of P_d, which will lead to the advance transition and separation of the flow, so the groove structure needs to be arranged in the front section. On the other hand, the back section of the surface already exhibits separated boundary layers and turbulent vortices, the ribs closer to the vortex have a more significant impact on the flow of the vortex. The ribs are arranged in the back section of the blade suction surface to optimize the lifting effect on the vortex. The results of drag reduction performance on micro-textured surfaces are shown in Table 4.

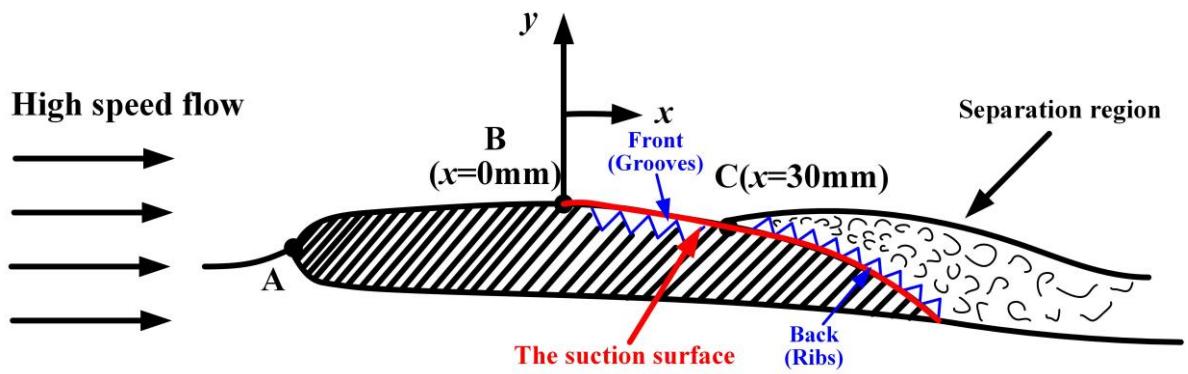

Figure 13: Schematic diagram of the micro-texture position on the suction surface.

Table 4: Simulation results of different type micro-textures in different regions on blade suction surface.

Group	Region	Type	*h* (mm)	*w* (mm)	*s* (mm)	*DR* (%)	η_ξ (%)
Case 1	Front	Groove	0.1	*w*(=*h*)	*s*(=*h*)	0.23	1.70
Case 2	Front	Groove	0.2	*w*(=*h*)	*s*(=*h*)	6.52	26.88
Case 3	Front	Groove	0.3	*w*(=*h*)	*s*(=*h*)	18.36	42.13
Case 4	Back	Rib	0.1	*w*(=*h*)	*s*(=*h*)	-1.31	-1.37
Case 5	Back	Rib	0.2	*w*(=*h*)	*s*(=*h*)	-1.17	-1.43
Case 6	Back	Rib	0.3	*w*(=*h*)	*s*(=*h*)	-1.16	-1.09

Table 4 shows that adding micro-texture changes the force on the blade. Compared with the back section of the suction surface, the drag increase and loss coefficient changes caused by the micro-texture arrangement in the front section are more pronounced. Case 1 to Case 3 indicates an increase in system energy loss without drag reduction effect. Moreover, a linear relationship exists between the rate of drag change and the height of the micro-texture, as the height directly influences the projected area and surface area. Regarding the rib located in the back section of the blade, it does exhibit a drag-reduction effect. Furthermore, the drag reduction performance of the rib in this area is independent of its height.

The surface pressure distribution situation in the front end of the textured blade suction is shown in Figure 14 (a). It is evident that the groove substantially influences the pressure distribution, with more significant impact observed as the height of the micro-texture increases. Conversely, the pressure distribution trend of the groove surface with a height of 0.1mm resembles that of a smooth one. Therefore, the groove has little effect on the drag and energy loss coefficient.

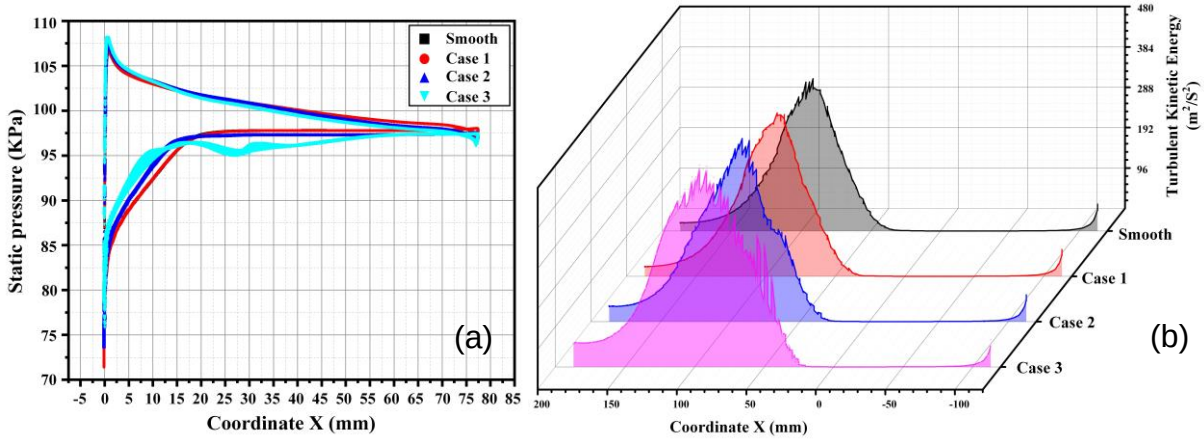

Figure 14: (a) Static pressure and (b) turbulent kinetic energy distribution of blade surface with different parameters of groove.

According to Figure 14 (b), the groove arranged in the front section of the blade suction surface leads to an increase in turbulent kinetic energy. It results in an earlier increase in turbulence intensity, indicating the premature separation of the boundary layer and an associated increase in energy loss. From both the perspective of resistance changes and energy loss, the groove does not effectively contribute to drag reduction performance.

From Table 4, the micro-texture is arranged in the back suction section of the blade surface, which explicitly affects drag reduction and loss coefficient. In order to explore the drag reduction characteristics of ribs on the back, the rib parameters are further analyzed. The specific simulation results are shown in Table 5.

Table 5: Simulation results of rib with different parameters arranged at the back section of blade surface.

Group	Region	Type	*h* (mm)	*w* (mm)	*s* (mm)	*DR* (%)	η_ξ (%)
Case 4	Back	Rib	0.1	*w*(=*h*)	*s*(=*h*)	-1.31	-1.37
Case 5	Back	Rib	0.2	*w*(=*h*)	*s*(=*h*)	-1.17	-1.43
Case 6	Back	Rib	0.3	*w*(=*h*)	*s*(=*h*)	-1.16	-1.09
Case 7	Back	Rib	0.2	*w*(=0.5*h*)	*s*(=*h*)	-1.30	-1.13
Case 8	Back	Rib	0.2	*w*(=1.5*h*)	*s*(=*h*)	-1.31	-1.45
Case 9	Back	Rib	0.2	*w*(=1.5*h*)	*s*(=*0*)	-1.19	-1.23
Case 10	Back	Rib	0.2	*w*(=1.5*h*)	*s*(=0.5*h*)	-1.15	-1.09

As shown in Figure 15 (a), it can be found that the resistance increases with the height of the ribs. However, this relationship is not linear and is influenced by the coupling effect of the micro-texture on P_d and F_d. The highest drag reduction, at 1.31%, is achieved when *h*=0.1mm, while the lowest loss coefficient is observed when *h*=0.2mm. As shown in Figure 15 (b), the drag reduction rate is the highest when *w*=1.5*h*, basically the same when *w*=0.5*h*. And the loss coefficient is the highest when *w*=1.5*h*. We therefore select Case 8, 9, and 10 (*w*=1.5*h*) to research the spacing parameter further. According to Figure 15 (c), the spacing exhibits the same effect on the drag reduction rate and energy loss coefficient. Moreover, the drag reduction effect is optimal when s=*h*.

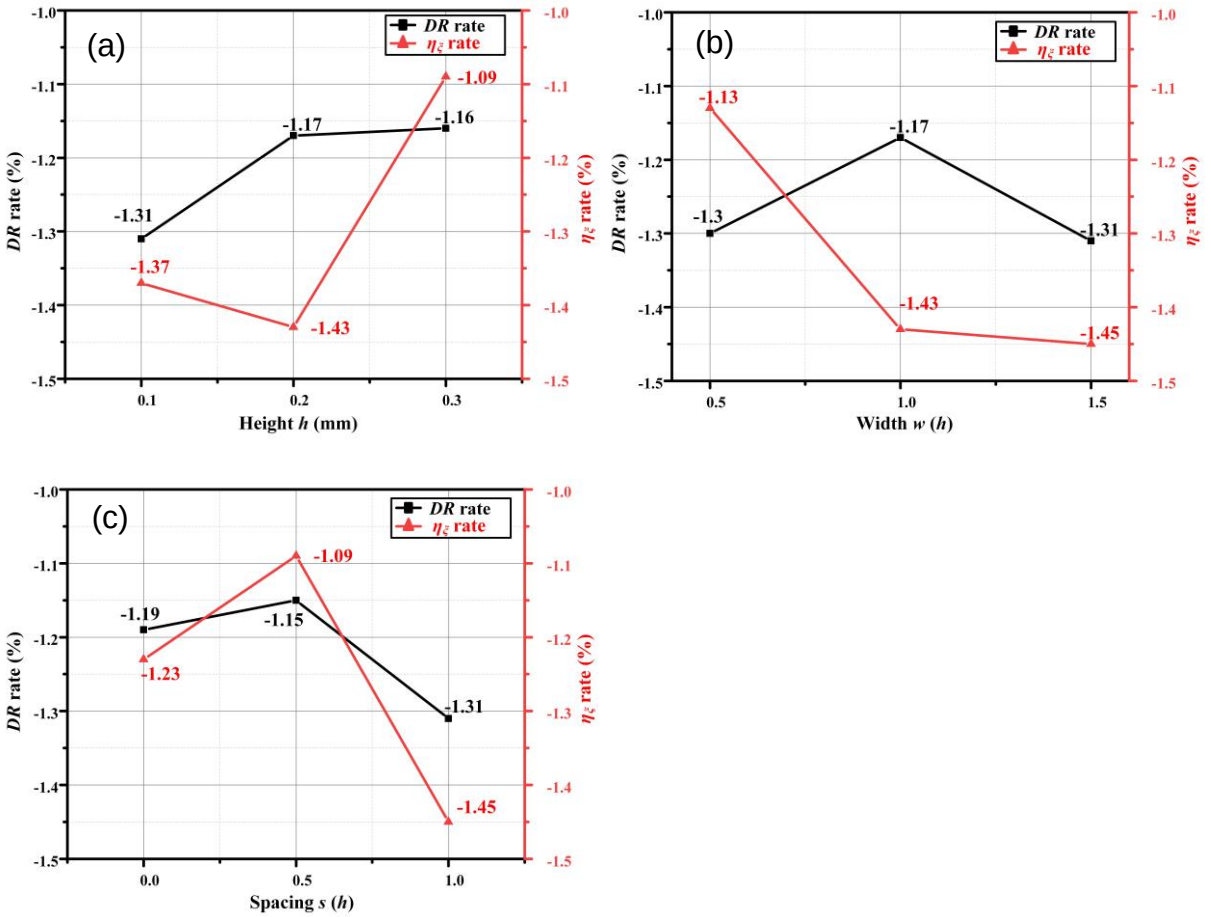

Figure 15: Influence of (a) height, (b) width, and (c) spacing of micro-textures on drag reduction performance.

The *DR* rate alone cannot fully represent the overall energy consumption for the entire impeller system. Thus we comprehensively consider the two simulation results to guide the micro-texture design. The selection criterion is based on achieving the smallest energy loss coefficient and the highest drag reduction rate. Following this standard, the rib with h=0.2mm, w=0.3mm, and s=0.2mm (case 8) has the best performance. Although the maximum drag reduction rate of a single blade is only 1.31%, and the energy loss coefficient decreases by 1.45%, its drag reduction effect remains significant for the whole impeller system with 45 blades.

The drag reduction mechanism analysis

The effective method to reduce drag in the flow field is to delay boundary layer separation and inhibit turbulence generation [30]. Because turbulence generation leads to energy dissipation, increasing the energy loss. Therefore, the drag reduction of the micro-textured blade surface is analyzed by considering turbulent kinetic energy, eddy viscosity ratio, and flow field. Figure 16 (a) compares smooth blades and textured blades (case 8) regarding the turbulence in the surrounding flow field. The presence of micro-texture on the blade surface results in a decrease in turbulent kinetic energy at the back end of the blade, thereby reducing energy losses. Figure 16 (b) compares the eddy viscosity ratio, representing the stress generated by turbulent motion. The red ellipse marks in the figures indicate that micro-texture significantly reduces the stress generated by turbulent motion. As a result, the energy loss in the entire flow channel system is substantially reduced.

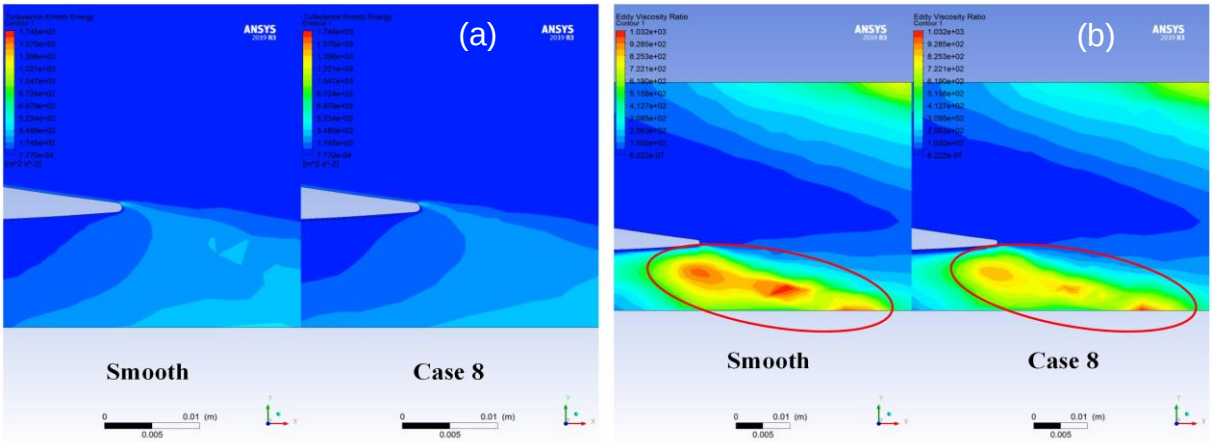

Figure 16: The effect of micro-texture on (a) turbulent kinetic energy and (b) eddy viscosity ratio around blades. Images used courtesy of ANSYS, Inc.

The influence of micro-texture on turbulent vortices is shown in Figure 17, the contour shows the pressure distribution in the flow domain. The periodic boundary is used in two pictures as the streamline release entrance, with identical streamline. Thus, it can

be seen from the streamline that the micro-texture effectively inhibits the turbulence generation and reduces system energy consumption. The weakening of turbulence will cause the reduction of wall shear stress, which is reflected in the reduction of friction resistance.

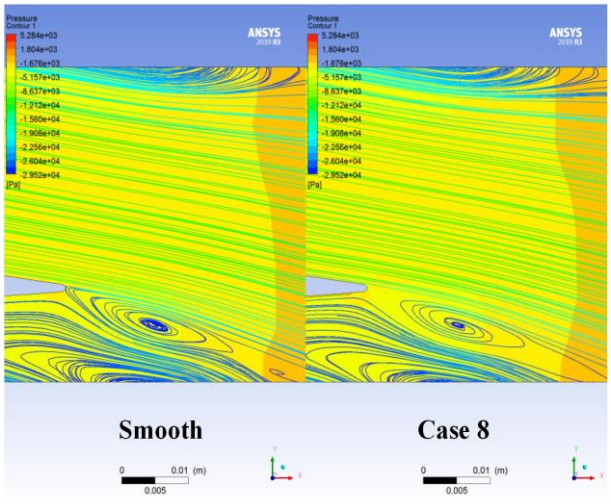

Figure 17: The effect of micro-texture on turbulent vortex. Image used courtesy of ANSYS, Inc.

The shear stress distribution on the smooth blade and micro-textured blade is shown in Figure 18 (a), the blue mark indicates that the placement of micro-textures does not change the overall shear stress distribution of the blade. Instead, it generates shear stress fluctuations within the micro-textured area. As shown in Figure 18 (b), the shear stress experiences significant fluctuations on the micro-textured surface, with the average shear stress being lower than the smooth surface. By calculation, the average value of shear stress decreases by 41.67%.

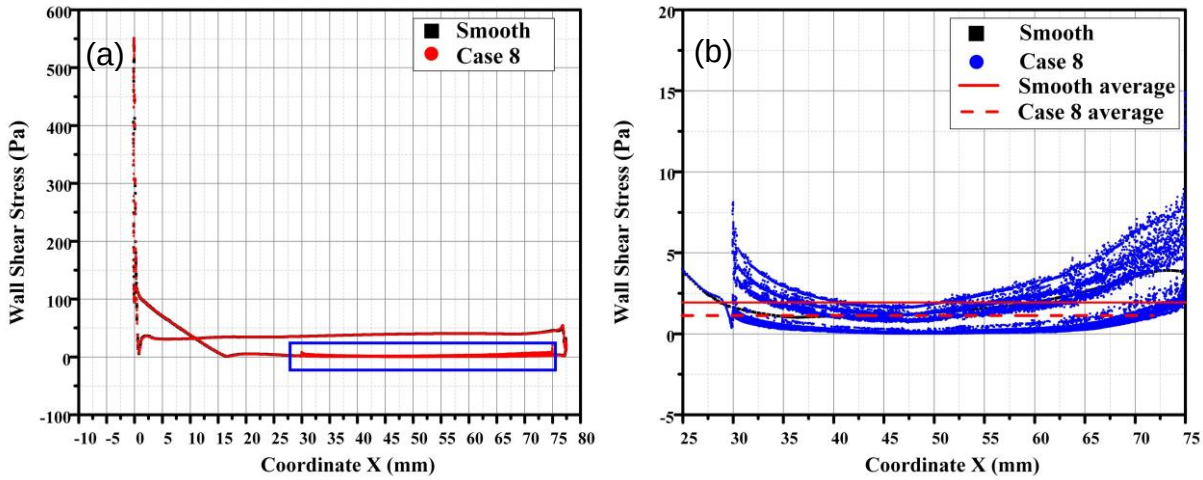

Figure 18: (a) Overall shear stress distribution and (b) local shear stress distribution of smooth and micro-textured blade.

Experimental

This chapter is written in two parts. The first one introduces the experimental equipment used in the micro-texture processing and wind tunnel experiments, and the second one describes the experiment process and the related results in detail.

Experimental equipment

The experimental process is divided into blade surface micro-texture machining and wind tunnel test. The list of equipment used in the experiment is shown in Table 6.

Table 6: Overview of the equipment used in the experiment

Equipment Name	Model	Purpose	Manufacturer
Five-axis CNC machine tool	JDGR400-A13S	Processing for blades and micro-textures.	Beijing Jingdiao Technology Group Co., LTD, China.

Flat end mill tool	Φ8*37*Φ8*81*3F[a]	Processing for blades.	Shanghai Mituo CNC Equipment Co., Ltd, China.
Ball end mill	Φ0.3*0.6*Φ4*50*2F[a]	Roughing for micro-textures.	MISUMI (China) Precision Machinery Trading Co., Ltd.
Ball end mill	Φ0.2*0.3*Φ4*50*2F[a]	Finishing for micro-textures.	MISUMI (China) Precision Machinery Trading Co., Ltd.
Trinocular stereo microscope	JSZ6S	Observe the processed blades.	Nanjing Jinsong Optical Instrument Co., Ltd, China.
Three-dimensional video microscope	KH-7700	High precision 3D imaging.	QUESTAR Corporation, Japan
The intermittent wind tunnel	Customized equipment	Blade aerodynamic performance test.	Nanjing Power Tiger Electromechanical Technology Co., Ltd, China.

[a]Φ(tool diameter/ mm)*(cutting edge length/ mm)*Φ(shank diameter)*(overall length/ mm)*(number of flutes)F.

Wind tunnel experiment of micro-textured blade surface

Micro-structure processing of blade surface

Based on the analysis of the simulation results, the micro-texture is arranged on the back end of the blade suction surface. The JDGR400-A13S five-axis CNC machine tool (Beijing Jingdiao Group) is used to process the blade and micro-textures, the processing steps are shown in Figure 19 (a). First, the blank of the blade is installed on the machine tool, the size of the blank is 140 (*h*)×100 (*l*)×25 (*w*)mm. Secondly, the end milling tool is used to mill the blank roughly to improve the processing efficiency. Thirdly, the high-quality blade models are obtained by finishing after the rough model of the blade is obtained. Finally, the micro-texture machining on the blade surface is divided into roughing and finishing, because the end milling tool will be broken if the tool with a smaller radius is used to process the micro-texture directly. The tool parameters used in different processing stages are shown in Table 7.

Table 7: Tool parameters in different machining stages.

Stages	Tools	Tool radius (mm)	Number of flutes
Roughing for blade	Flat end mill	4	3
Finishing for blade	Flat end mill	4	3
Roughing for micro-texture	Ball end mill	0.15	2
Finishing for micro-texture	Ball end mill	0.1	2

The processed blade, composed of 7075 series aluminium alloy, is displayed in Figure 19 (b). The blade surface quality is assessed using the JSZ6S trinocular stereo microscope, the results showed that the processed blade have high quality and without

obvious defects. In order to further analyse the processing quality, the HIROX KH-7700 three-dimensional video microscope is used to examine the micro-texture and blade surface morphology, as shown in Figure 20.

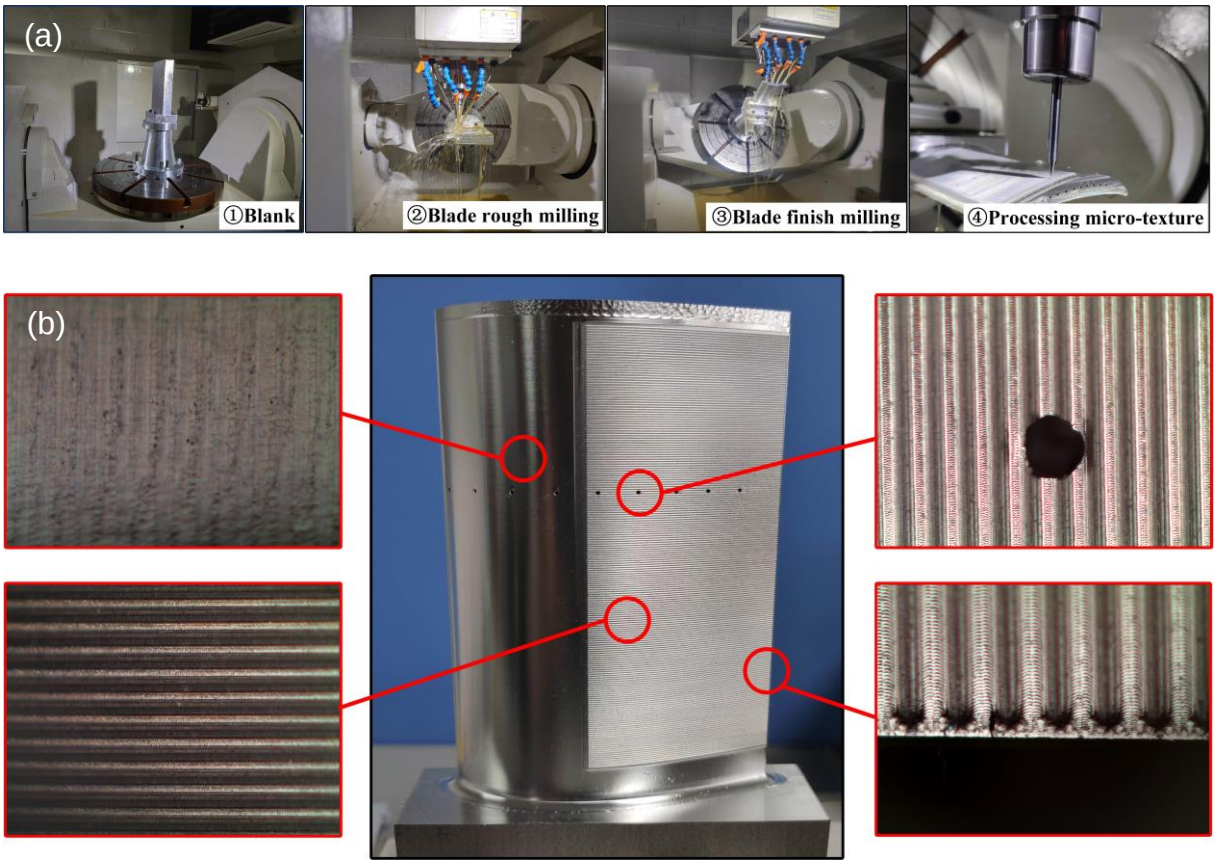

Figure 19: The processing of micro-textured blade. (a) The manufacturing procedure of the micro-textured blade. (b) The processed blade with micro-textures.

The rib surface morphology and dimensional data are shown in Figure 20 (a). The theoretical height is 0.2mm, the width is 0.3mm, the spacing is 0.2mm, and the rib-tip spacing is 0.5mm, while the actual height measures 0.202mm and the rib-tip spacing is 0.534mm. The machining error is minimal due to the utilization of a ball end milling tool with a diameter of 0.2mm, which has a processing residue at the corner of the bottom rib area shown in Figure 21 (a). Figure 20 (b) indicates slight height fluctuations on the surface of the smooth blade, reaching a maximum deviation of 0.007mm. This occurrence can be attributed to the point contact nature of the ball tip tool during the

machining process and the spacing between tool paths. Thus the machining coverage rate does not reach 100%, resulting in residual height (*h*), as shown in Figure 21 (b). To sum up, the micro-texture processed this time meets the quality requirements.

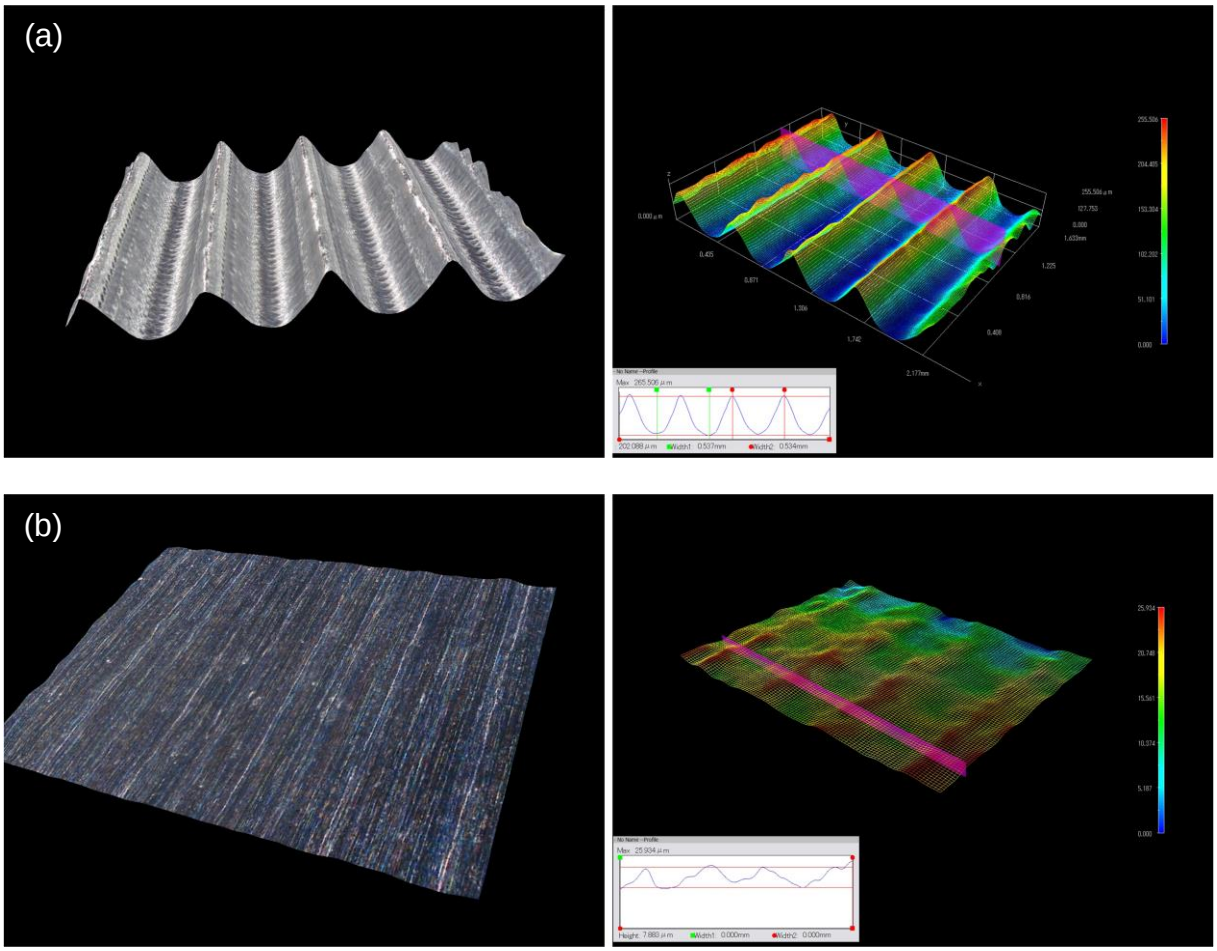

Figure 20: Microscope observation of the processed (a) micro-rib surface morphology and (b) blade surface morphology.

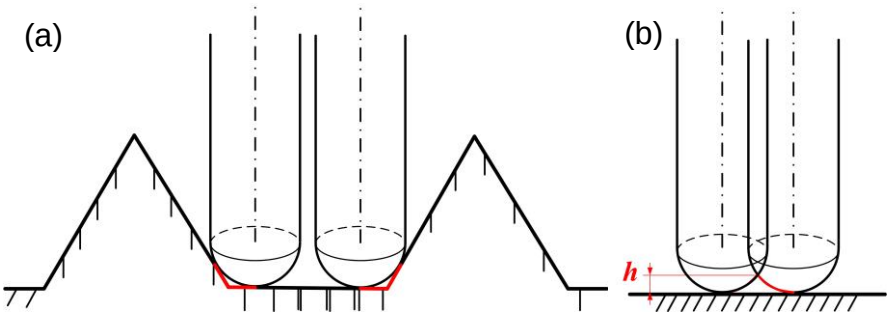

Figure 21: The machining error analysis diagram of (a) the micro-texture and plane processing.

Experimental platform

The experiment was conducted in the intermittent wind tunnel at the College of Energy and Power Engineering, Nanjing University of Aeronautics and Astronautics. The pictures and schematic diagram of the wind tunnel test platform are shown in Figure 22. Figure 22 (b) shows that the wake measurement device comprises a three-hole probe, a motor, and a guide rail. 10 probes are utilized to measure the wake, while the motor facilitates control and adjustment of their position. The total pressure (*TP*), static pressure (*P*) and velocity of the air flow (*V*) in the experiment were obtained by the three-hole probe measuring device. These three results can be calculated according to Eq. (5)-(8) to obtain the results of *Ma* and ξ. The airflow angle can be set by controlling the motor and thus turning the disc, where can be seen in Figure 22 (c). In Figure 22 (c), the inlet of the test platform is connected with the high-pressure gas source, which is 100m^3 high-pressure gas tank with a maximum of 25atm; the air extraction source is a 200m^3 vacuum tank with a minimum of 0.1atm.

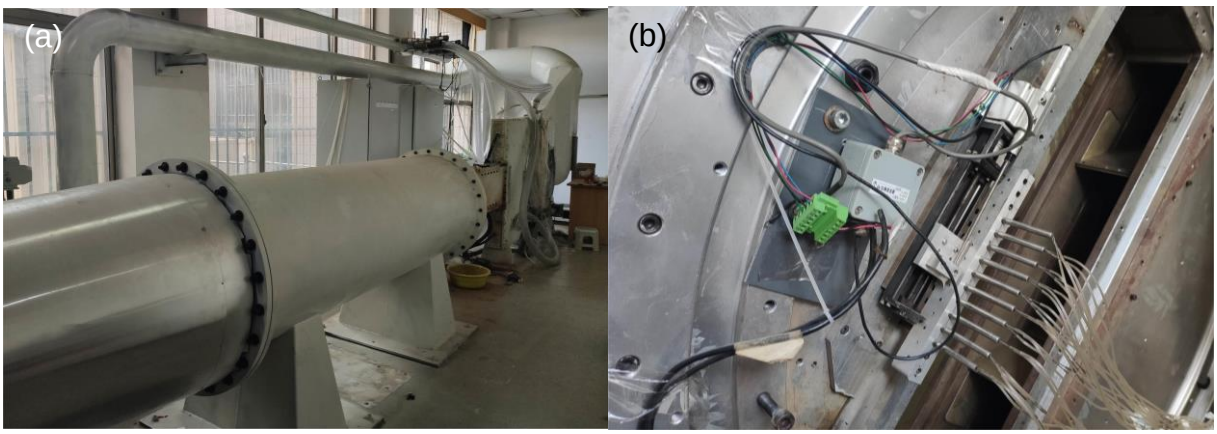

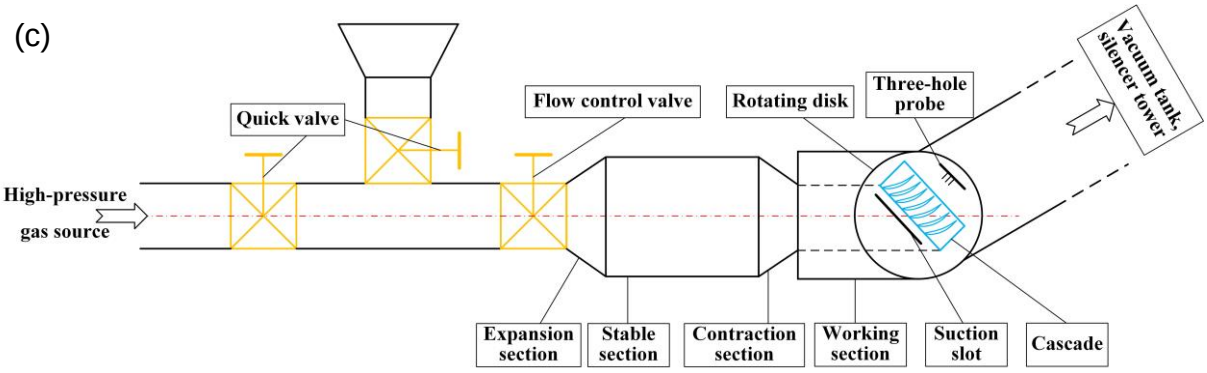

Figure 22: Experimental platform and schematic diagram. (a) The wind tunnel test platform. (b) Three-hole probe measuring device. (c) Schematic diagram of the wind tunnel test platform.

Experimental steps and results

To ensure the accuracy of experiments, the velocity and airflow angles of 0.25, 0.5, and 0.75 blade height were selected to carry out multiple tests to verify the drag reduction effect of the micro-textured blade. The specific steps of the experiment are as follows:

(1) Prepare two blades in contrast: one smooth blade and the other blade with micro-texture on the surface;

(2) Testing the smooth blade first: adjust the wind tunnel flow velocity to 123.98m/s and the airflow angle to 52.8°；

(3) Measurement of the *TP* and *P* at the inlet and outlet, respectively. Calculation of the ξ and observation of the wake loss distribution;

(4) Change the velocity to 130.67m/s, airflow angle to 54.8°, and proceed to Step (3)；

(5) Change the velocity to 137.54m/s, airflow angle to 57.0°, and proceed to Step (3)；

(6) Replace the blades with micro-texture and repeat Steps (3), (4), and (5). The experimental results are shown in Table 8 and Table 9.

Table 8: Experimental results of the inlet and outlet of the smooth blade.

Airflow angle /°	TP_1 (Pa)	P_1 (Pa)	TP_2 (Pa)	P_2 (Pa)	V_1[a] (m/s)	V_2[b] (m/s)	ξ_0[c]
52.8	108055.8	98762.9	105010.2	100920.1	123.66	91.56	41.61%
54.8	109091.3	98832.9	104266.1	101070.6	129.50	69.00	58.98%
57.0	111401.5	99905.3	104646.6	101292.4	135.91	70.21	65.45%

[a]Inlet velocity; [b]Outlet velocity; [c]Energy loss coefficient of the smooth blade.

Table 9: Experimental results of the inlet and outlet of the micro-textured blade.

Airflow angle /°	TP_1 (Pa)	P_1 (Pa)	TP_2 (Pa)	P_2 (Pa)	V_1[a] (m/s)	V_2[b] (m/s)	ξ_1[c]
52.8	108840.2	99248.2	105190.1	101131.2	125.23	79.23	46.17%
54.8	109810.1	99392.6	104571.2	101268.8	130.10	69.38	60.09%
57.0	110852.6	99359.3	104828.0	101488.0	136.24	69.87	63.02%

[a]Inlet velocity; [b]Outlet velocity; [c]Energy loss coefficient of the micro-textured blade.

Table 8 presents the results indicating that the ξ_0 rises with increased airflow angle. The simulation reveals distinct phenomena occurring at three airflow angles, the separation phenomenon and vortex at the back section on blade become more apparent and intense with the increase of angle. From Table 9, the textured blade has a more significant effect on reducing the ξ_1 as the flow angle increases. At the flow angle of 57°, the η_ξ reduces by 3.7%. Thus, the micro-texture reduces energy consumption and improves the overall aerodynamic performance of blades.

Figure 23 and 24 illustrate the distribution of the LC_{TP} and outlet *Ma* at three different airflow angles. A higher LC_{TP} and lower *Ma* indicate the poorer aerodynamic

performance of the blade. According to Figure 23 (a) and 24 (a), the blade with micro-texture exhibits an increase in LC_{TP} from 0.4 to 0.5, while the *Ma* in the flow channel centre decreases from 0.2 to 0.13. These results indicate that at the flow angle of 52.8°, the micro-texture has an adverse effect on the aerodynamic performance of the blade, resulting in increased drag. From Figure 23 (c) and 24 (c), the blade with micro-texture experiences a smaller LC_{TP} compared to the smooth blade, and the *Ma* is slightly higher. These results indicate a reduction in system energy loss. Overall, the micro-texture arranged in the back section of the blade positively impacts aerodynamic performance and reduces system energy loss, particularly at an airflow angle of 57°.

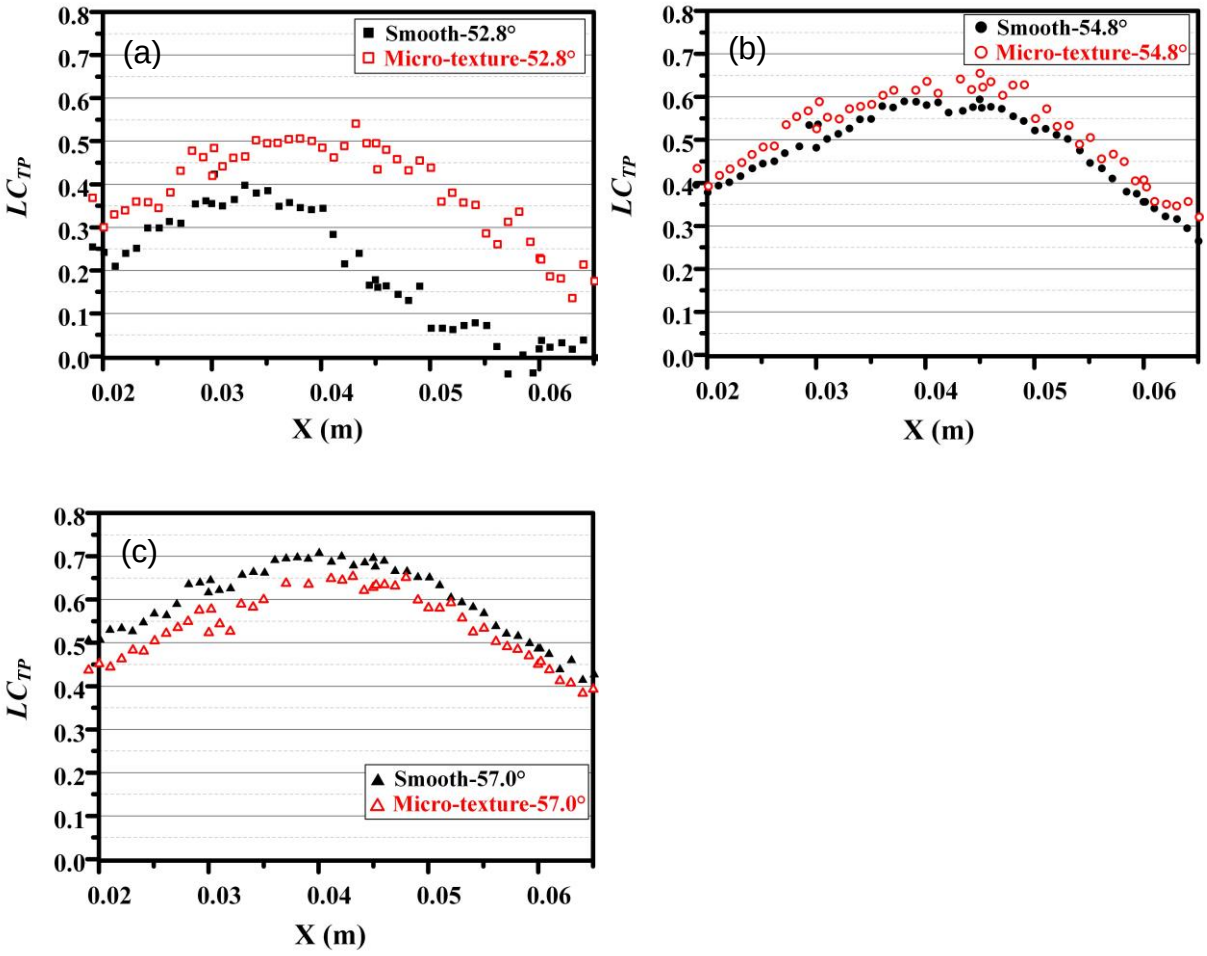

Figure 23: Distribution of LC_{TP} of single flow channel at the airflow angle of (a) 52.8°, (b) 54.8°, and (c) 57.0°.

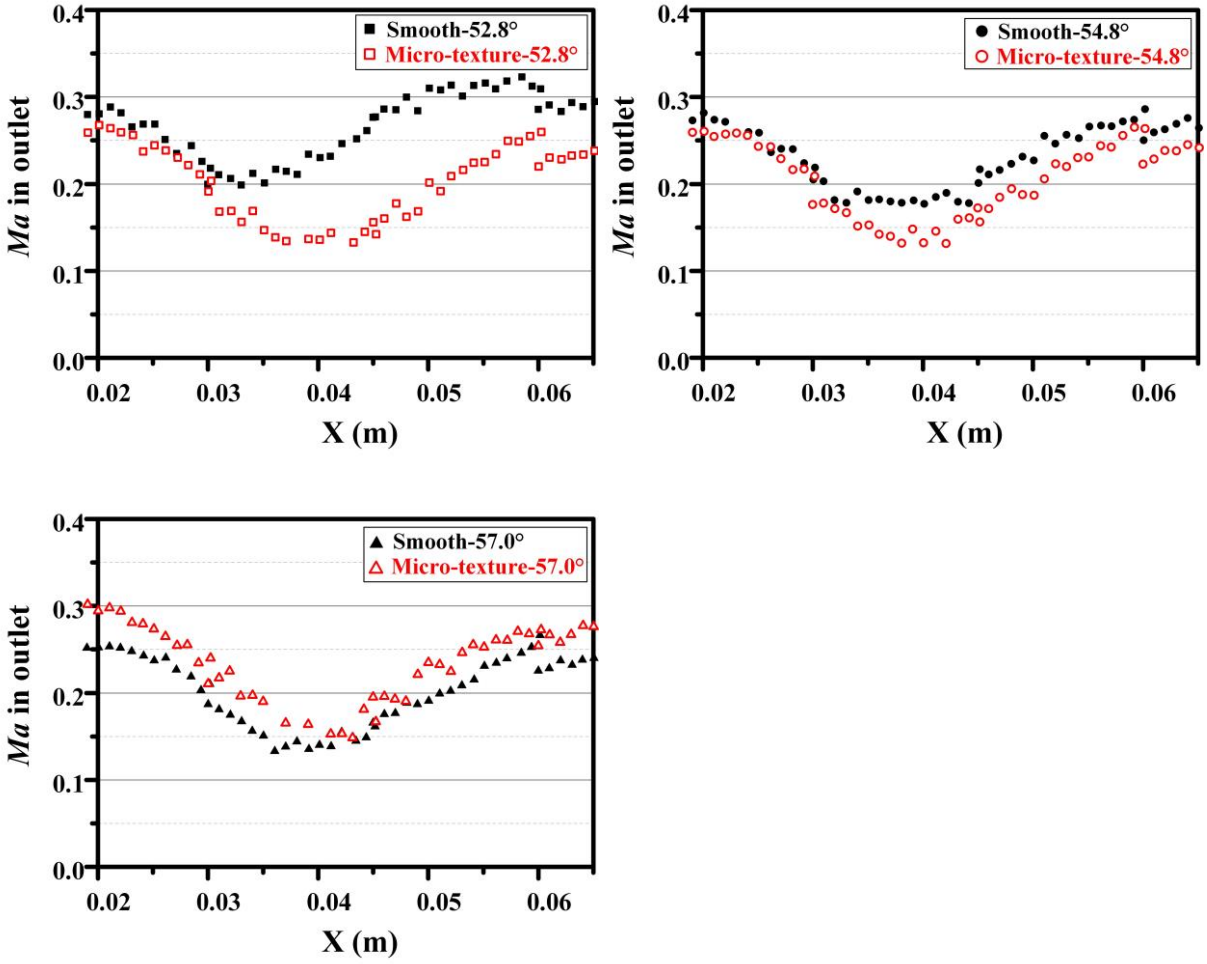

Figure 24: Distribution of *Ma* of single flow channel at the airflow angle of (a) 52.8°, (b) 54.8°, and (c) 57.0° in outlet.

The micro-texture is arranged at the back end of the blade suction surface based on the analysis of the simulation results, and the drag reduction effect of the micro-texture is verified in the wind tunnel experiment. As shown in Figure 25, the drag reduction performance of the micro-texture blade is the best when the airflow angle is 57°, the η_ξ can reach 2.43% and the simulation result under this condition is 3.7%. Although the difference between the simulation results and the experimental results is large under the other two attack angles, the change trend of the η_ξ of the two is the same. The larger the airflow angle, the smaller the η_ξ.

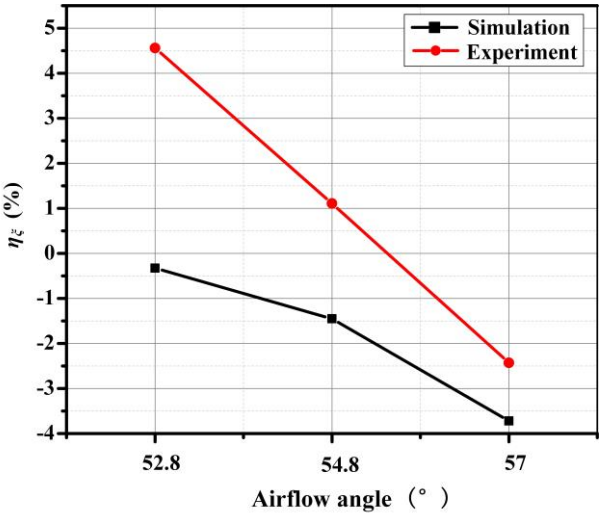

Figure 25: Comparison between the simulation value and the experimental value of the η_ξ.

Conclusion

This paper studies an axial flow compressor and presents a simplified numerical simulation method for the rotating blade surface. Furthermore, the micro-texture design and simulation analysis are carried out on blade surface to explore the drag reduction mechanism of micro-texture. The conclusions are as follows:

(1) A simplified simulation method is proposed from the whole to a single impeller, establishing the relationship between the plane and surface. Theoretical calculations and numerical simulations are employed to design and verify the optimal micro-texture for drag reduction performance. The determined micro-texture dimensions include a height of 0.2mm, a width of 0.3mm, and a spacing of 0.2mm.

(2) The drag reduction mechanism is analyzed and compared for micro-textures with different geometric size factors. The presence of micro-textures on the blade surface effectively impedes turbulence generation, thus reducing the turbulent kinetic energy and wall shear stress to reduce drag.

(3) The simulation results reveal that positioning the optimally sized microstructure at the back end of the blade yields significant benefits. The *DR* rate for a single blade reaches 1.31%, accompanied by a reduction of 1.45% in the η_{ξ}. Moreover, the average shear stress of the micro-texture surface is decreased by 41.67%.

(4) A blade cascade experiment is conducted in the high-speed wind tunnel to analyze the energy loss coefficient and wake loss distribution. The results demonstrate a reduction in energy consumption of 2.43% at the flow velocity of 136.24 m/s and the attack angle of 57°.

Acknowledgements

Thanks go to Professor Zhenggui Zhou and his team, who provided the intermittent wind tunnel for this paper. They are from the College of Energy and Power Engineering, Nanjing University of Aeronautics and Astronautics.

References

1. Carreño Ruiz, M.; D'Ambrosio, D. *Aerosp. Sci. Technol.* **2023,** *132*. doi:10.1016/j.ast.2022.108047

2. Liu, W.; Ni, H.; Wang, P.; Zhou, *Y. Beilstein J. Nanotech.* **2020,** *11,* 24–40. doi:10.3762/bjnano.11.3

3. Bixler, G. D.; Bhushan, B. *Adv. Funct. Mater*. **2013,** *23*, 4507–4528. doi:10.1002/adfm.201203683

4. Bhushan, B. *Beilstein J. Nanotech.* **2011,** 66–84. doi:10.3762/bjnano.2.9

5. Walsh, M. Turbulent Boundary Layer Drag Reduction Using Riblets. 20th Aerospace Sciences Meeting, Orlando, FL, U.S.A. January 11-14, 1982; American Institute of Aeronautics and Astronautics (AIAA). doi:10.2514/6.1982-169

6. Bechert, D. W.; Bartenwerfer, M. *J. Fluid Mech.* **1989,** *206*, 105–129. doi:10.1017/S0022112089002247

7. Huang, H.; Zhang, Y.; Ren, L. *J. Bionic Eng.* **2012,** *9*, 465–469. doi:10.1016/S1672-6529(11)60141-8

8. Martin, S.; Bhushan, B. *RSC Adv.* **2016,** *6*, 10962–10978. doi:10.1039/c5ra20944g

9. Bearman, P. W.; Harvey, J. K. *AIAA J.* **1993,** 31, 1753–1756. doi:10.2514/3.11844

10. Choi, K. so. *J. Fluid Mech.* **1989,** *208*, 417–458. doi:10.1017/S0022112089002892

11. Bixler, G. D.; Bhushan, B. *J. Colloid Interf. Sci.* **2013**, *393*, 384–396. doi:10.1016/J.JCIS.2012.10.061

12. García-Mayoral, R.; Jiménez, J. *J. Fluid Mech.* **2011**, *678*, 317–347. doi:10.1017/JFM.2011.114

13. García-Mayoral, R.; Jiménez, J. *Philosophical Transactions of the Royal Society A: Mathematical, Phys. Eng. Sci.* **2011**, *369*, 1412–1427. doi:10.1098/RSTA.2010.0359

14. Chamorro, L. P.; Arndt, R. E. A.; Sotiropoulos, F. *Renew. Energ.* **2013**, *50*, 1095–1105. doi:10.1016/J.RENENE.2012.09.001

15. Zhang, C.; Saurav Bijay, K. *Aerosp. Sci. Technol.* **2018**, *72*, 380–396. doi:10.1016/J.AST.2017.11.007

16. Spalding DB. *J. Appl. Mech.* **1961,** *28*, 4555-458. https://doi.org/10.1115/1.3641728.

17. Kline, S. J.; Reynolds, W. C.; Schraub, F. A.; Runstadler, P. W. *J. Fluid Mech.* **1967**, *30*, 741–773. doi:10.1017/S0022112067001740

18. Robinson, S. K. *Annu. Rev. Fluid Mech.* **1991**, *23*, 601-639. https://doi.org/10.1146/annurev.fl.23.010191.003125.

19. Zhu, W.; Bons, J.; Gregory, J. *Exp. Fluids* **2023**, *64*. doi:10.1007/s00348-022-03550-2

20. White, F. *Viscous Fluid Flows*; 2005; Vol. 20. doi:10.1016/S0997-7546(00)01113-4

21. Hon, T.-L.; Walker, J. *An Analysis of the Motion and Effects of Hairpin Vortices*; 1987; Vol. 1

22. Robinson, S. K. A Review of Vortex Structures and Associated Coherent Motions in Turbulent Boundary Layers. Structure of Turbulence and Drag Reduction, Zurich, Switzerland, July 25–28, 1989; IUTAM Symposium. doi:10.1007/978-3-642-50971-1_2

23. Denton, J. D. LOSS MECHANISMS IN TURBOMACHINES. International Gas Turbine and Aeroengine Congress and Exposition, Cincinnati, Ohio, May 24-27,1993; The American Society of Mechanical Engineers. https://doi.org/10.1115/93-GT-435

24. Li, C.; Li, X.; Li, P.; Ye, X. *Energy* **2014**, *75*, 534–548. doi:10.1016/j.energy.2014.08.015

25. Kueh, T. C.; Beh, S. L.; Ooi, Y. S.; Rilling, D. G. Experimental Study to the Influences of Rotational Speed and Blade Shape on Water Vortex Turbine Performance. In Journal of Physics: Conference Series; Institute of Physics Publishing, 2017; 822. doi:10.1088/1742-6596/822/1/012066

26. Song, Z.; Zheng, X.; Wang, B.; Zhou, K.; Amankwa Adjei, R. *Aerosp. Sci. Technol.* **2023**, *136*, 108187. doi:10.1016/J.AST.2023.108187

27. Wu, Z.; Li, S.; Liu, M.; Wang, S.; Yang, H.; Liang, X.; *Eng. Appl. Comp. Fluid.* **2019,** *13*, 1024-1035. doi:10.1080/19942060.2019.1665101

28. Raayai-Ardakani, S.; McKinley, G. H. *Phys. Fluids* **2019**, *31*. doi:10.1063/1.5090881

29. Walsh, M. J. *AIAA J.* **1983**, *21*, 485. doi:10.2514/3.60126

30. Raayai-Ardakani, S.; McKinley, G. H. *Phys. Fluids* **2017**, *29*. doi:10.1063/1.4995566